



# Evidence of a Decreased Binary Fraction for Massive Stars within 20 milliparsecs of the Supermassive Black Hole at the Galactic Center

Devin S. Chu<sup>1</sup> , Tuan Do<sup>1</sup> , Andrea Ghez<sup>1</sup> , Abhimat K. Gautam<sup>1</sup> , Anna Ciurlo<sup>1</sup> , Kelly Kosmo O'Neil<sup>1</sup> , Matthew W. Hosek, Jr.<sup>1,6</sup> , Aurélien Hees<sup>2</sup> , Smadar Naoz<sup>1,3</sup> , Shoko Sakai<sup>1</sup> , Jessica R. Lu<sup>4</sup> , Zhuo Chen (陈卓)<sup>1</sup> ,

Rory O. Bentley<sup>1</sup> , Eric E. Becklin<sup>1</sup>, and Keith Matthews<sup>5</sup>

<sup>1</sup> Department of Physics and Astronomy, UCLA, Los Angeles, CA 90095-1547, USA; [dchu@astro.ucla.edu](mailto:dchu@astro.ucla.edu)

<sup>2</sup> SYRTE, Observatoire de Paris, Université PSL, CNRS, Sorbonne Université, Paris, France

<sup>3</sup> Mani L. Bhaumik Institute for Theoretical Physics, Department of Physics and Astronomy, UCLA, Los Angeles, CA 90095-1547, USA

<sup>4</sup> Astronomy Department, University of California, Berkeley, Berkeley, CA 94720, USA

<sup>5</sup> Department of Physics and Astronomy, Caltech, Pasadena, CA 91125, USA

Received 2022 October 7; revised 2023 March 17; accepted 2023 March 29; published 2023 May 11

## Abstract

We present the results of the first systematic search for spectroscopic binaries within the central  $2 \times 3$  arcsec $^2$  around the supermassive black hole at the center of the Milky Way galaxy. This survey is based primarily on over a decade of adaptive optics-fed integral-field spectroscopy ( $R \sim 4000$ ), obtained as part of the Galactic Center Orbits Initiative at Keck Observatory, and it has a limiting  $K$ -band magnitude of 15.8, which is at least 4 mag deeper than previous spectroscopic searches for binaries at larger radii within the central nuclear star cluster. From this primary data set, over 600 new radial velocities are extracted and reported, increasing by a factor of 3 the number of such measurements. We find no significant periodic signals in our sample of 28 stars, of which 16 are massive, young (main-sequence B) stars and 12 are low-mass, old (M and K giant) stars. Using Monte Carlo simulations, we derive upper limits on the intrinsic binary star fraction for the young star population at 47% (at 95% confidence) located  $\sim 20$  mpc from the black hole. The young star binary fraction is significantly lower than that observed in the field (70%). This result is consistent with a scenario in which the central supermassive black hole drives nearby stellar binaries to merge or be disrupted, and it may have important implications for the production of gravitational waves and hypervelocity stars.

*Unified Astronomy Thesaurus concepts:* Galactic center (565); Infrared spectroscopy (2285); Adaptive optics (2281); Binary stars (154)

*Supporting material:* machine-readable tables

## 1. Introduction

The closest known stars to the Milky Way's supermassive black hole (SMBH) comprise the so-called "S-star" cluster, where S stands for Sgr A\*, the emissive source associated with the SMBH. This population is distinct, both dynamically and spectroscopically, from the surrounding stellar population. Spectroscopic observations have also revealed that most of these stars are main-sequence B stars (Ghez et al. 2003; Eisenhauer et al. 2005; Habibi et al. 2017). Unlike their cousins outside the central radius of 0.04 pc, this population lacks Wolf-Rayet stars, suggesting the S-stars have formed within the last 20 million years. Their young ages raise questions about their formation mechanism, given that traditional star formation would be disrupted by the tidal forces of the black hole (Morris 1993).

Numerous investigations have been done to postulate the formation of these S-stars. General mechanisms include: (1) binary star systems scattered from outside the region and then tidally disrupted, leaving behind one component of the original binary while the other is ejected as a hypervelocity star (e.g.,

Hills 1988; Perets et al. 2007; Generozov & Madigan 2020), (2) S-stars formed in the clockwise disk located just outside 1'' of the SMBH and then migrated to the SMBH (e.g., Levin 2007; Löckmann et al. 2008; Merritt et al. 2009), and (3) merger of binary stars at the Galactic centers caused by the Kozai–Lidov mechanism, with the product appearing as a main-sequence B-star (e.g., Witzel et al. 2014; Stephan et al. 2016; Fragione & Antonini 2019; Ciurlo et al. 2020).

Binary stars provide crucial roles in these formation mechanisms, and the discovery of binary stars among the S-stars may attest to particular formation mechanisms. Additionally, massive stars in the field have high multiplicity fractions (Sana et al. 2012; Duchêne & Kraus 2013), so it is reasonable to expect these main-sequence B stars at least started out in multiple systems (Naoz et al. 2018). Previous studies have identified three binary systems (Ott et al. 1999; Martins et al. 2006; Rafelski et al. 2007; Pfahl et al. 2014; Gautam et al. 2019), but none among the S-stars. Chu et al. (2018) performed the first spectroscopic search for binaries among the S-stars and focused on the well-studied star S0-2 (also known as S2). Through radial velocity monitoring, Chu et al. (2018) did not find significant evidence for S0-2 being a binary, and they placed a hypothetical companion mass upper limit at  $1.6 M_{\odot}$ , which is below current detection limits. The data set that was used to analyze S0-2 can be used to perform a more comprehensive survey.

In this work, we use the Galactic Center Orbits Initiative (GCOI; PI Ghez, W. M. Keck Observatory 1995–present) long-

<sup>6</sup> Brinson Prize Fellow.

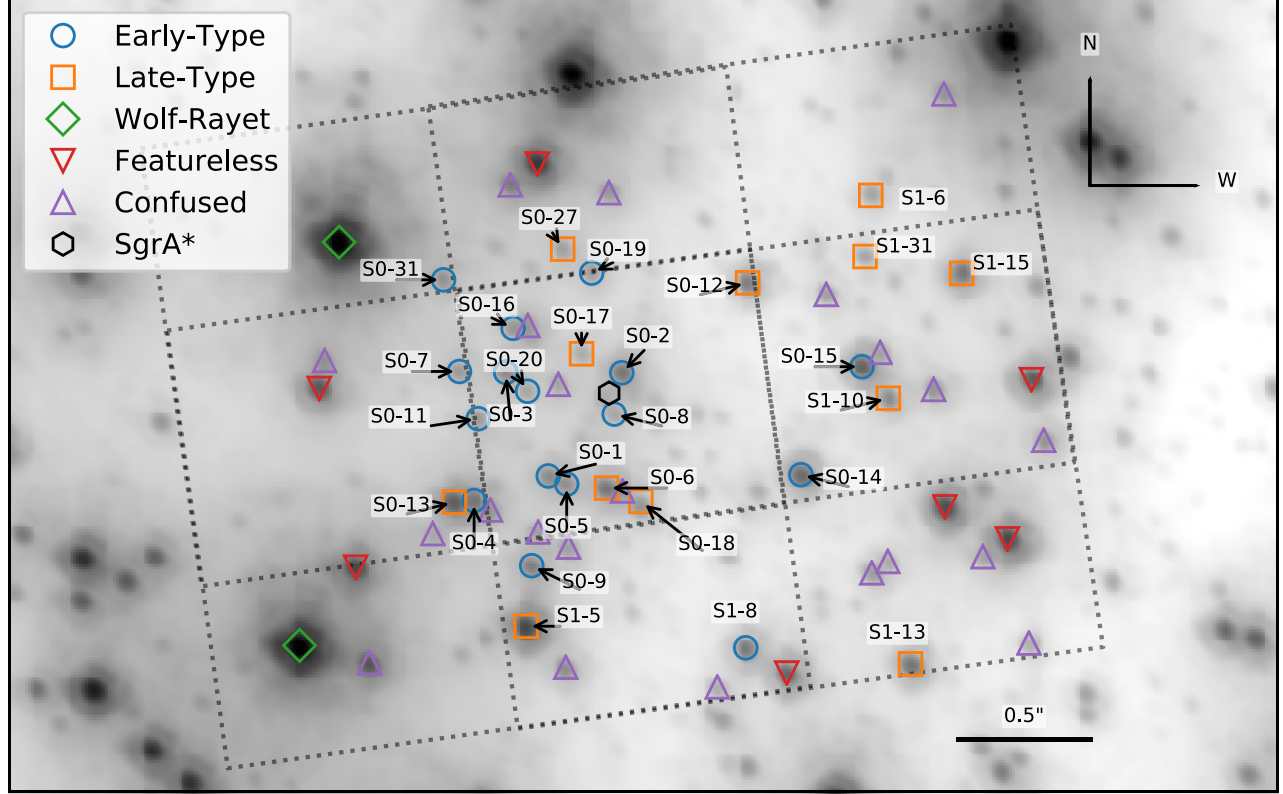


**Figure 1.** Finding chart for stars included in the periodicity search. The GCOI’s OSIRIS four-pointing outer dither pattern is overlaid on an adaptive optics  $2.2\ \mu\text{m}$  Keck NIR2 image of the Galactic center. Most of the sample is located in the central pointing dither pattern (blue circles: early-type, orange squares: late-type). The central square is covered by all dither points, meaning more spectra are taken of these stars throughout the night. We include all stars brighter than  $K = 16$  mag, except Wolf-Rayet stars (green diamond), stars lacking absorption lines (red triangle), or stars that are confused with other stellar sources or gas features (purple triangle).

term monitoring of this region with W. M. Keck Observatory to conduct a systematic search for binary stars using radial velocities of the S-stars. This paper is organized as follows. Section 2 details the sample selection process for this search. Section 3 describes the radial velocity data used in searching for spectroscopic binaries. Section 4 details the process of modeling the long-term motion of the sample stars around the central black hole. Section 5 describes the search methodology for looking for companion stars in the stellar sample. Section 6 provides an overview of placing an upper limit on the binary star fraction. Section 7 discusses how these limits carry implications for the evolution of the S-stars.

## 2. Sample Selection

The broadest criteria of the star sample used in the analysis presented in this paper is that the star must be brighter than  $K' > 16$  mag and located within the field of view of this study’s primary data set, which is centered on S0-2 and covers  $3'' \times 2''$  at a PA of  $285^\circ$  (see Figure 1, Table 1, and Section 3). Our magnitude limit stems from what can be measured with an adequate signal-to-noise ratio from a single night of observations ( $\sim 3\text{--}4$  hr of integration). These initial criteria yield an intermediate sample of 62 stars. From here, we make several other cuts. First, Wolf-Rayet emission line sources (IRS16C and IRS16SW) are excluded because measuring their radial velocities is complicated due to their stellar winds. Similarly, the seven main-sequence O stars are excluded because they are featureless across the spectral range studied ( $2.121\text{--}2.229\ \mu\text{m}$ ). We further omit 25 stars for which source confusion prevents

their radial velocities from being extracted without bias in our primary data set (see Appendix A for details). We also omit the star S0-28 because it only has two radial velocity measurements, which is too few to conduct a periodicity search. This leads to a final sample of 28 stars, of which 16 are early-type stars and 12 are late-type stars (see Table 2).

## 3. Radial Velocities

### 3.1. New Radial Velocities

The primary starting point for the radial velocity analysis is the spectrally calibrated data sets that have been used by the Galactic Center Orbits Initiative (GCOI) to study S0-2 (see references in Table 1). The majority of these observations were taken with the OSIRIS spectrograph ( $R \sim 4000$ , Larkin et al. 2006) on the W. M. Keck 10 m Telescope using the laser guide star adaptive optics (LGSAO) system (van Dam et al. 2006; Wizinowich et al. 2006) and reduced via the OSIRIS reduction pipeline (Lyke et al. 2017; Lockhart et al. 2019). These 45 data sets were taken in the 35 mas pixel scale and through the Kn3 ( $2.121\text{--}2.229\ \mu\text{m}$ ) filter, which covers the Br $\gamma$  absorption line ( $\lambda = 2.166\ \mu\text{m}$ ) for the young stars and Na for the old stars. With a  $2 \times 2$  dither pattern that keeps the central  $1'' \times 1''$  in the field of view, a total view of  $3'' \times 2''$  is achieved (see Figure 1). Over the course of the reported observations, OSIRIS has gone through the following two upgrades: (1) a grating upgrade in December 2012 (Mieda et al. 2014) and (2) a detector upgrade in April 2016 (Boehle et al. 2016b). Appendix B shows the impact of the detector upgrade on our data set (the grating upgrade had no significant effect). Of the 45 data sets with

**Table 1**  
Summary of Spectroscopic Observations with New Radial Velocities

Date <sup>a</sup> (UT)	Date <sup>a</sup> (MJD)	Date <sup>a</sup> (Epoch)	Instrument	$N_{\text{frames}} \times t_{\text{int}}$ (s)	Filter	Scale (mas)	FWHM <sup>b</sup> (mas)	S/N <sup>b</sup>	New RVs This Work <sup>c</sup>
2005-07-03 <sup>1</sup>	53554.50	2005.503	OSIRIS	7 × 900	Kbb	20	58	44	5
2006-06-18 <sup>1</sup>	53904.50	2006.461	OSIRIS	9 × 900	Kn3	35	81	39	10
2006-06-30 <sup>1</sup>	53916.50	2006.494	OSIRIS	9 × 900	Kn3	35	77	42	12
2006-07-01 <sup>1</sup>	53917.50	2006.497	OSIRIS	9 × 900	Kn3	35	64	46	8
2007-05-21 <sup>1</sup>	54241.50	2007.384	OSIRIS	2 × 900	Kn3	35	86	16	5
2007-07-18 <sup>1</sup>	54299.29	2007.542	OSIRIS	2 × 900	Kn3	35	66 <sup>5</sup>	33 <sup>5</sup>	4
2007-07-19 <sup>1</sup>	54300.29	2007.545	OSIRIS	2 × 900	Kn3	35	56	32	6
2008-05-16 <sup>2</sup>	54602.50	2008.372	OSIRIS	11 × 900	Kn3	35	57	66	17
2008-07-25 <sup>2</sup>	54672.28	2008.563	OSIRIS	9 × 900	Kn3	35	81	57	17
2009-05-05 <sup>2</sup>	54956.50	2009.342	OSIRIS	7 × 900	Kn3	35	70	58	18
2009-05-06 <sup>2</sup>	54957.50	2009.344	OSIRIS	12 × 900	Kn3	35	81	74	9
2010-05-05 <sup>2</sup>	55321.50	2010.341	OSIRIS	6 × 900	Kn3	35	70	26	8
2010-05-08 <sup>2</sup>	55324.50	2010.349	OSIRIS	11 × 900	Kn3	35	79	43	19
2011-07-10 <sup>2</sup>	55752.33	2011.520	OSIRIS	6 × 900	Kn3	35	71	29	20
2011-07-19 <sup>2</sup>	55761.31	2011.545	OSIRIS	6 × 900	Kn3	35	96 <sup>6</sup>	27 <sup>6</sup>	7
2012-06-11 <sup>2</sup>	56089.50	2012.444	OSIRIS	7 × 900	Kn3	20	64	40	4
2012-07-22 <sup>2</sup>	56130.31	2012.555	OSIRIS	7 × 900	Kn3	35	92	37	10
2012-08-12 <sup>2</sup>	56151.33	2012.613	OSIRIS	6 × 900	Kn3	35	56	66	6
2012-08-13 <sup>2</sup>	56152.27	2012.615	OSIRIS	7 × 900	Kn3	35	99	41	8
2013-05-11 <sup>2</sup>	56423.50	2013.358	OSIRIS	11 × 900	Kbb	35	73	41	7
2013-05-12 <sup>2</sup>	56424.50	2013.361	OSIRIS	11 × 900	Kbb	35	62	45	3
2013-05-13 <sup>2</sup>	56425.50	2013.363	OSIRIS	12 × 900	Kbb	35	61	33	3
2013-05-14 <sup>2</sup>	56426.50	2013.366	OSIRIS	11 × 900	Kn3	35	67	72	21
2013-05-16 <sup>2</sup>	56428.50	2013.372	OSIRIS	7 × 900	Kn3	20	98	53	5
2013-05-17 <sup>2</sup>	56429.50	2013.374	OSIRIS	7 × 900	Kn3	20	64	43	5
2013-07-25 <sup>2</sup>	56498.33	2013.563	OSIRIS	11 × 900	Kn3	35	79	35	8
2013-07-26 <sup>2</sup>	56499.34	2013.566	OSIRIS	6 × 900	Kn3	35	73	22	5
2013-07-27 <sup>2</sup>	56500.33	2013.568	OSIRIS	11 × 900	Kn3	35	72	49	18
2013-08-10 <sup>2</sup>	56514.29	2013.607	OSIRIS	7 × 900	Kn3	35	62	50	13
2013-08-11 <sup>2</sup>	56515.31	2013.609	OSIRIS	9 × 900	Kn3	35	69	24	14
2013-08-13 <sup>2</sup>	56517.29	2013.615	OSIRIS	12 × 900	Kn3	35	67	54	11
2014-05-17	56794.51	2014.374	OSIRIS	6 × 900	Kn3	35	69 <sup>6</sup>	41 <sup>6</sup>	6
2014-05-18 <sup>3</sup>	56795.50	2014.376	OSIRIS	13 × 900	Kn3	35	66	53	18
2014-05-19	56796.51	2014.379	OSIRIS	13 × 900	Kn3	35	65 <sup>6</sup>	62 <sup>6</sup>	20
2014-05-22	56799.51	2014.387	OSIRIS	7 × 900	Kn3	35	82 <sup>6</sup>	26 <sup>6</sup>	6
2014-05-23 <sup>3</sup>	56800.50	2014.390	OSIRIS	10 × 900	Kn3	35	76	42	8
2014-07-03 <sup>3</sup>	56841.36	2014.502	OSIRIS	8 × 900	Kn3	35	66	57	22
2015-05-04 <sup>3</sup>	57146.50	2015.337	OSIRIS	5 × 900	Kn3	35	77	49	4
2015-07-21 <sup>3</sup>	57224.35	2015.551	OSIRIS	5 × 900	Kn3	35	56	51	24
2015-08-07	57241.33	2015.597	OSIRIS	2 × 900	Kn3	35	84 <sup>7</sup>	13 <sup>7</sup>	1
2016-05-14 <sup>3</sup>	57522.50	2016.367	OSIRIS	8 × 900	Kbb	35	78	58	1
2016-05-15 <sup>3</sup>	57523.50	2016.370	OSIRIS	4 × 900	Kbb	35	80	36	2
2016-05-16 <sup>3</sup>	57524.50	2016.372	OSIRIS	8 × 900	Kbb	35	84	63	2
2016-07-11	57580.35	2016.525	OSIRIS	8 × 900	Kbb	35	69 <sup>8</sup>	42 <sup>8</sup>	6
2016-07-12	57581.33	2016.528	OSIRIS	7 × 900	Kbb	35	115 <sup>9</sup>	30 <sup>9</sup>	1
2017-05-17 <sup>4</sup>	57890.52	2017.374	OSIRIS	11 × 900	Kn3	35	73	101	20
2017-05-18 <sup>4</sup>	57891.51	2017.377	OSIRIS	9 × 900	Kn3	35	94	49	20
2017-05-19 <sup>4</sup>	57892.50	2017.379	OSIRIS	6 × 900	Kn3	35	86	77	8
2017-07-19 <sup>4</sup>	57953.33	2017.546	OSIRIS	12 × 900	Kn3	35	77	55	10
2017-07-27 <sup>4</sup>	57961.32	2017.568	OSIRIS	13 × 900	Kn3	35	89	76	20
2017-08-14 <sup>4</sup>	57979.28	2017.617	OSIRIS	8 × 900	Kn3	35	75	71	21
2018-03-17 <sup>4</sup>	58194.64	2018.207	OSIRIS	2 × 900	Kn3	35	70	30	6
2018-04-24 <sup>4</sup>	58232.57	2018.310	OSIRIS	7 × 900	Kn3	35	73	67	12
2018-05-13 <sup>4</sup>	58251.51	2018.362	NIFS	12 × 600	K	50 × 100		84	7
2018-05-22 <sup>4</sup>	58260.49	2018.387	NIFS	7 × 600	K	50 × 100		66	4
2018-05-23 <sup>4</sup>	58261.50	2018.390	OSIRIS	14 × 900	Kn3	35	91	97	19
2018-06-05 <sup>4</sup>	58274.47	2018.425	OSIRIS	10 × 900	Kn3	35	108	44	4
2018-07-22 <sup>4</sup>	58321.33	2018.554	OSIRIS	11 × 900	Kn3	35	77	113	18
2018-07-31 <sup>4</sup>	58330.32	2018.578	OSIRIS	11 × 900	Kn3	35	73	121	16
2018-08-11 <sup>4</sup>	58341.31	2018.608	OSIRIS	9 × 900	Kn3	35	79	121	19

**Notes.** Col 1–3: date of observation given in UT, modified Julian date, and Julian Year. Col 4: instrument name. Col 5: number of frames combined, times the exposure time of each frame. Col 6: instrument filter. Col 7: pixel scale used. Col 8: FWHM of reference star, Col 9: spectral signal-to-noise ratio of reference star. Col 10: new radial velocity measurements reported.

<sup>a</sup> These observations, where noted, were first reported for studies of S0-2 alone in the following references: (1) Ghez et al. (2008), (2) Boehle et al. (2016a), (3) Chu et al. (2018), and (4) Do et al. (2019).

<sup>b</sup> The reported values are assessed on S0-2 unless otherwise noted as follows: (5) S1-15, (6) S0-14, (7) S1-13, (8) S0-3, and (9) S0-12. All stars used for characterization have  $K'$  mag of 13.5–14.5.

<sup>c</sup> This includes only RVs for the final sample.

**Table 2**  
S-star RV Sample

Star	$K'$ (mag)	Spectral Type	R.A. $\Delta^a$ ( $''$ )	Decl. $\Delta^a$ ( $''$ )	R2D $a$ ( $''$ )	RV Points	[RV $\sigma$ ] (km s $^{-1}$ )	RV Baseline (Years)	RV Long-term Trend Method	Semimajor Axis (mpc)
S0-1	14.7	Early	0.04	-0.26	0.264	50	53	15	Orbit	$24.43 \pm 0.46$
S0-2	14.0	Early	-0.01	0.17	0.172	115	23	18	Orbit	$4.885 \pm 0.024$
S0-3	14.5	Early	0.34	0.12	0.356	59	37	14	Orbit	$14.082 \pm 0.082$
S0-4	14.1	Early	0.45	-0.33	0.558	52	46	15	Orbit	$16.39 \pm 0.66$
S0-5	15.0	Early	0.17	-0.36	0.408	42	61	14	Orbit	$10.678 \pm 0.067$
S0-7	15.1	Early	0.51	0.10	0.524	23	30	12	Polynomial	$39.9 \pm 8.0$
S0-8	15.8	Early	-0.23	0.16	0.274	45	95	14	Orbit	$16.612 \pm 0.089$
S0-9	14.2	Early	0.22	-0.60	0.625	33	36	13	Polynomial	$69 \pm 14$
S0-11	15.1	Early	0.49	-0.06	0.505	28	32	12	Polynomial	$103 \pm 21$
S0-14	13.5	Early	-0.76	-0.28	0.811	41	18	12	Polynomial	$48.7 \pm 9.7$
S0-15	13.5	Early	-0.97	0.18	0.984	31	32	12	Polynomial	$54 \pm 11$
S0-16	15.3	Early	0.23	0.17	0.284	24	76	14	Orbit	$11.611 \pm 0.062$
S0-19	15.3	Early	-0.08	0.40	0.404	39	120	15	Orbit	$11.581 \pm 0.040$
S0-20	15.8	Early	0.05	0.14	0.153	32	200	14	Orbit	$10.260 \pm 0.033$
S0-31	14.9	Early	0.57	0.45	0.711	9	41	11	Polynomial	$57 \pm 11$
S1-8	14.0	Early	-0.58	-0.92	1.088	16	33	11	Polynomial	$89 \pm 18$
S0-6	14.0	Late	0.02	-0.36	0.356	47	2.9	13	Polynomial	$102 \pm 20$
S0-12	14.3	Late	-0.55	0.41	0.689	48	3.1	12	Polynomial	$115 \pm 23$
S0-13	13.2	Late	0.56	-0.41	0.691	48	2.9	12	Polynomial	$82 \pm 16$
S0-17	15.9	Late	0.05	0.008	0.048	44	90	15	Orbit	$13.639 \pm 0.090$
S0-18	14.9	Late	-0.12	-0.42	0.441	18	4.0	12	Polynomial	$73 \pm 15$
S0-27	15.5	Late	0.15	0.55	0.566	12	5.6	12	Polynomial	$52 \pm 10$
S1-5	12.4	Late	0.32	-0.89	0.943	27	2.6	12	Polynomial	$150 \pm 30$
S1-6	15.4	Late	-0.96	0.74	1.217	19	7.7	10	Polynomial	$163 \pm 33$
S1-10	14.7	Late	-1.10	-0.02	1.099	22	5.2	12	Polynomial	$116 \pm 23$
S1-13	14.0	Late	-1.14	-0.97	1.501	7	5.2	12	Polynomial	[158]
S1-15	14.0	Late	-1.36	0.49	1.443	23	3.9	11	Polynomial	[152]
S1-31	15.6	Late	-0.99	0.54	1.125	16	7.6	11	Polynomial	[118]

**Notes.** Col 1: star name. Col 2: magnitude in  $K'$ . Col 3–5: projected distance from SgrA\*. Col 6: total radial velocity points used in analysis. Col 7: median radial velocity uncertainty. Col 8: baseline of radial velocity measurements. Col 9: method for subtracting long-term RV trend. Col 10: semimajor axes estimates (values in brackets come from averaging comparably large separations).

<sup>a</sup> From Sgr A\*.

(This table is available in machine-readable form.)

newly reported radial velocities, four observations are newly reported here: 2014 May 17, 2014 May 19, 2014 May 22, and 2015 August 7 UT. The three nights in 2014 May do not contain S0-2 radial velocity measurements, due to noise spikes affecting the spectra of that star. For the night of 2015 August 7, a field south of the central pointing was observed, which meant S0-2 was not in the field of view, but the star S1-13 was in the dither, which is on the southern edge of the central pointing. On average, the observations have a FWHM of 76 mas and a spectral signal-to-noise ratio of 53 for a 14 mag star.

Several data sets supplement the above core data. Thirteen of these data sets are also taken with OSIRIS, at a different plate scale (20 mas) and/or through the broader Kbb filter (1.965–2.381  $\mu\text{m}$ ). Of these, two are new observations that have not been previously published. These two Kbb observations were taken on 2016 November 7 and 2016 December 7 UT. On these nights, weather and dithering problems prevented S0-2 from being observed, but other stars in the sample were still in the field of view. We also include a number of previously published data sets taken with other instruments, including Keck NIRSPEC ( $R \sim 2800$  in low-resolution mode), Keck NIRCam ( $R \sim 4000$ ), Gemini North NIFS ( $R \sim 5000$ ; McGregor et al. 2003), and Subaru IRCS ( $R \sim 20,000$ ). A

summary of all the spectroscopic observations with new radial velocities is reported in Table 1.

### 3.2. Extracting Radial Velocities

Previous papers from the UCLA GCOI reported the radial velocities of S0-2 and S0-38. In this work, we also extracted the radial velocities of other known stars located in the central pointing. The methods and calibrations used to measure radial velocities are reported in Do et al. (2019).

To summarize, a star’s spectrum is extracted from the individual data cubes from a given epoch using a circular aperture, with an annulus around the star to estimate the sky background. The spectra are then averaged into a combined spectrum. The star’s combined spectrum is then modeled using the Bayesian inference tool Starkit (Kerzendorf & Do 2015) and compared to spectra in the BOSZ spectral grid (Bohlin et al. 2017). The radial velocity and its uncertainty are derived using the median and  $1\sigma$  central credible interval of the marginalized posterior. Do et al. (2019) showed that this technique of spectral fitting reduced uncertainties and systematic bias compared to fitting a Gaussian to the Br $\gamma$  line for the star S0-2. Example spectra and their model fits for both early- and late-type stars are shown in Figure 2. Early-type stars are main-sequence B stars, with the Br $\gamma$  absorption line being the

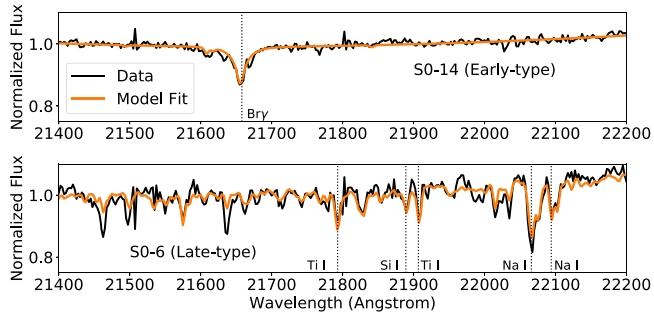


**Figure 2.** Example spectra and model fits for the early-type star S0-14 (top) and the late-type star S0-6 (bottom). Br $\gamma$  absorption is the primary spectral feature for early-type stars in the OSIRIS Kn3 filter, while the late-type stars have more features. The multiple absorption line features in late-type stars lead to increased precision for their radial velocity measurements compared to early-type stars.

major spectral feature in the Kn3 filter. Late-type stars are M and K giants with many absorption lines in Kn3, notably the Na doublet lines around 22,100 Å. The measured radial velocity is then corrected for the local standard of rest with respect to the Galactic center.<sup>7</sup>

We apply this same technique to all the other stars in the OSIRIS data when a star's radial velocity can be measured. The number and quality of radial velocity measurements extracted for each epoch depends greatly on a number of factors, such as weather conditions, adaptive optics performance, and position in the OSIRIS dither pattern. Stellar crowding and confusion can also lead to difficulties when extracting a radial velocity measurement. Even though a star may be identified in an OSIRIS cube, its spectrum may not be of adequate quality to measure its radial velocity. We perform a quality inspection of the extracted spectra to ensure their radial velocities can be measured.

In this work, we report 626 new radial velocity measurements. To this, we add the 344 radial velocities from the literature (Gillessen et al. 2017; Do et al. 2019), the majority of which are for S0-2. As Figure 3 shows, the new RV measurements dramatically increase ( $\sim 3$  times) the coverage for other stars in this region, enabling the first binary star population study.

#### 4. Modeling the Long-term Motion around the SMBH

Some of the stars in the selected sample have significant long-term motion from their orbits around the SMBH, which we model and remove as a necessary initial step for conducting a periodic search for binary stars. For the 10 stars that have orbital periods around the SMBH of less than 180 yr (a semimajor axis less than 24 mpc) and have gone through a turning point during our observations, we have enough astrometry and radial velocities in the GCOI database to directly model their orbital motions. For the shortest-period and best-studied star, S0-2, we use the orbital model reported in Do et al. (2019). This model also provides us with the black hole parameters (position, proper motion, mass, and distance to Earth), which we use as fixed values in our orbital model for the other short-period stars. For the short-period stars beyond

<sup>7</sup> We use the IRAF procedure rvcorrect. This correction uses a velocity of 20 km s $^{-1}$  for the solar motion with respect to the local standard of rest in the direction  $\alpha = 18^{\text{h}}$ ,  $\delta = +30^{\circ}$  for epoch 1900 (Kerr & Lynden-Bell 1986), corresponding to  $(u, v, w) = (10, 15.4, 7.8)$  km s $^{-1}$ .

**Table 3**  
Polynomial Fit Results

Star	$t_0$ (Epoch)	$v_{z0}$ (km s $^{-1}$ )	$a_z^{\text{a}}$ (km s $^{-1}$ yr $^{-1}$ )	$\chi^2_{\text{red}}$
S0-7	2014.4978	$105.3 \pm 5.9$	[6.9]	3.3
S0-9	2014.3799	$114.5 \pm 4.8$	[4.1]	2.1
S0-11	2014.2696	$-22.2 \pm 4.6$	[4.7]	1.5
S0-14	2013.8235	$-31.3 \pm 2.8$	[2.2]	1.0
S0-15	2013.6498	$-552.5 \pm 4.8$	[4.1]	2.9
S0-31	2012.5771	$-118.9 \pm 10.6$	[9.3]	1.7
S1-8	2012.2612	$-112 \pm 7.2$	[5.9]	1.9
S0-6	2013.6093	$90.4 \pm 0.42$	$0.83 \pm 0.12$	1.7
S0-12	2013.9746	$-39.3 \pm 0.48$	[0.44]	2.0
S0-13	2013.9545	$-45.1 \pm 0.41$	[0.35]	2.2
S0-18	2014.4520	$-289.3 \pm 1.0$	[1.0]	3.5
S0-27	2013.8851	$-121.2 \pm 1.5$	[1.3]	4.3
S1-5	2014.4119	$11.2 \pm 0.50$	[0.38]	1.9
S1-6	2013.8535	$-42.0 \pm 1.5$	[1.7]	1.1
S1-10	2013.7375	$-33.6 \pm 1.0$	[0.77]	1.4
S1-13	2012.4453	$-749.1 \pm 1.6$	[1.2]	6.8
S1-15	2011.8983	$-120.4 \pm 0.82$	[0.65]	2.1
S1-31	2014.0749	$182.9 \pm 1.6$	[1.7]	1.9

Notes. Col 1: star name. Col 2:  $t_0$  epoch from polynomial radial velocity fit. Col 3: constant velocity offset. Col 4: acceleration parameter. Col 5:  $\chi^2_{\text{red}}$  of the fit.

<sup>a</sup> The  $3\sigma$  limits are given in brackets. The value is reported with its  $1\sigma$ .

(This table is available in machine-readable form.)

S0-2 with measurable orbits, we also fix the astrometric correlation length from source confusion to 30 mas and the radial velocity offset between the Keck and VLT measurements to 0 km s $^{-1}$  (see Do et al. 2019; Ciurlo et al. 2020). Leaving these values free has no impact on modeling the radial velocity curves or residuals. The seven modeled parameters for these stars are the six standard stellar orbital parameters (period, eccentricity, inclination, longitude of the ascending node, argument of periape, and epoch of closest approach) plus the astrometric mixing parameter. The star's semimajor axis and its uncertainty can also be obtained from its orbital period (and uncertainty) and black hole mass using Kepler's Third Law. Once the star's orbital fit is performed, a model for its radial velocity is generated and subtracted to create a residual curve. The last column of Table 2 provides the estimated semimajor axes for these short-period stars' motions around the SMBH.

For stars with longer orbital periods around the black hole, we performed a polynomial fit to their radial velocities. The degree of the polynomial fit is determined by the F-test, where a higher-degree polynomial must pass the F-test of the lower-degree polynomial with a 95% significance. Of the 18 stars fit with a polynomial, all but one are best fit with a constant radial velocity model, and one (S0-6) is fit well with a constant acceleration model. These polynomial fits are reported in Table 3. The polynomial fit is then subtracted from the radial velocity points to create residual points, which are reported in Table 4. An example of radial velocity and residual points are shown in Figure 4. For these longer-period stars, their semimajor axes are estimated using the same orbit fitting method described above. These estimates have formal uncertainties from 1% to 20%, and the lower value is most likely an underestimate due to the small orbital phase coverage; we therefore assign a 20% semimajor axis uncertainty for these stars. For three late-type stars on the edge of our sample, we

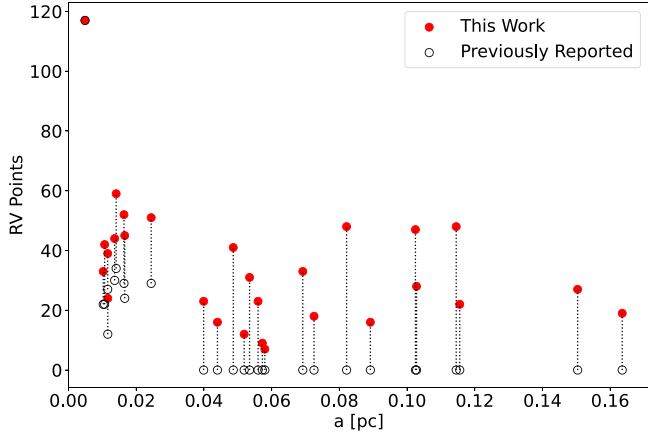


**Figure 3.** Number of radial velocity points for a star vs. its estimated semimajor axis. The number of previously published points is given by the unfilled gray circles, while the number of points used in this work is given in red. The dotted lines connect the points for visual increase. S0-2 is the star with the most radial velocity points, because of its brightness and close proximity to the black hole. This work reports 626 new radial velocity measurements.

were unable to obtain orbital solutions. To estimate their semimajor axes, we take the average of comparably large separations from the SMBH. These semimajor axes estimates are also reported in Table 2.

## 5. Companion Star Searches

The following section describes the process for detecting periodic signals in the radial velocity residual curves using two types of periodicity searches: a Lomb–Scargle analysis (Lomb 1976; Scargle 1982; VanderPlas 2018) and a Bayesian fit for potential binary systems. A similar methodology was done for the star S0-2 in Chu et al. (2018). The Lomb–Scargle analysis provides a computationally efficient method for detecting periodic signals in unevenly spaced data. The Bayesian fitting method provides a more complete and robust approach, and it allows us to derive upper limits on the orbital parameters of hypothetical binary companions to these S-stars.

### 5.1. Lomb–Scargle Analysis

Once a star’s residual radial velocity curve is made, it is run through a Lomb–Scargle package, `gatspy` (VanderPlas & Ivezić 2015; VanderPlas et al. 2016), to search for a periodic signal. When running this periodic search, a range of periods from 2 to 10,000 days are sampled. The lower period sampling limit of 2 days comes from the Nyquist sampling limit of taking data on consecutive days. The upper period limit of 10,000 days ensures that the entire time baseline of the data set is covered. To ensure that potential signals are not missed due to uniform sampling, the “ $N$  samples per peak” feature of the `gatspy` package is used. We specify  $N = 10$  samples per peak, which carries out 10 additional, finer samples around a peak in Lomb–Scargle power (see VanderPlas & Ivezić 2015; VanderPlas et al. 2016, for details). The periods are uniformly spaced at  $1/N\Delta t$ , where  $N$  is the samples per peak and  $\Delta t$  is the maximum time baseline of observations. Spacing the sampled periods at  $1/N\Delta t$  ensures proper sampling of a data set (VanderPlas 2018). Chu et al. (2018) calculated an upper limit of 119 days for the longest period for an S0-2 binary star system, as systems with longer periods would separate at S0-2’s closest approach to the SMBH. The stars in this sample are

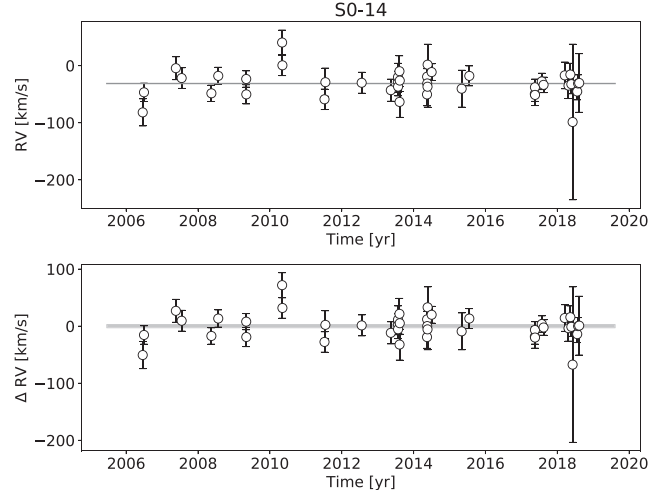


**Figure 4.** Top: Radial velocity of S0-14 over time. A model fit of polynomial order 0 is fit to the data. Bottom: Difference of measured radial velocity points from the model for S0-14. Uncertainty of the model fit is incorporated into the shaded region.

not expected to pass as close to the SMBH, hence they would have longer maximum periods, which is why we decided to increase the upper period sampled. After this step, a Lomb–Scargle power spectrum is obtained, containing power values for every sampled period. An example Lomb–Scargle periodogram for S0-14 is shown in Figure 5. Periodograms for the entire sample are given in Appendix C

The significance values of the peak Lomb–Scargle powers are determined in three ways: (i) comparing the Lomb–Scargle amplitude to the star’s radial velocity uncertainty, (ii) Monte Carlo simulation, and (iii) bootstrap false-alarm probability (FAP) test significance. Each of these methods produces a significance value between 0% and 100%, with the higher percentage corresponding to a higher significance. These three methods compliment one another, and a higher significance value means a higher likelihood that a binary system has been detected.

One way to evaluate the significance of the Lomb–Scargle power for each star is to look at the fit amplitude from the Lomb–Scargle model. The Lomb–Scargle analysis returns an amplitude of the sinusoid model fit to the residual curve. This amplitude is divided by the median radial velocity uncertainty for that star to determine the amplitude significance in terms of sigma. If a star’s residual has a very large amplitude of variation relative to its radial velocity uncertainty, the variation can be considered significant relative to noise.

The second way to determine significance is to use a Monte Carlo simulation. This Monte Carlo simulation is conducted in the same way as described in Chu et al. (2018). To summarize, 100,000 simulated residual curves with no periodic signal are generated for each star. Each simulated curve has the same observation times and uncertainties as the data. Every data point is drawn from a Gaussian distribution centered around 0  $\text{km s}^{-1}$ , meaning the simulated data contained no periodic signal and only noise. These simulated curves are then run through the Lomb–Scargle process described above, and the maximum Lomb–Scargle power for each run is recorded. A cumulative distribution function for the 100,000 simulations is compiled. The peak Lomb–Scargle power from the data is then compared to the cumulative distribution function. This approach allows us to quantify the significance of our peak

**Table 4**  
Radial Velocities and Residuals

Epoch (yr)	MJD	RV (km s <sup>-1</sup> )	RV $\sigma$ (km s <sup>-1</sup> )	Residual (km s <sup>-1</sup> )	Source	Reference
2006.461	53904.50	-81	23	-50	S0-14	
2006.497	53917.50	-46	16	-15	S0-14	
2007.384	54241.50	-4	20	26	S0-14	
...	...	...	...	...	...	...

**Notes.** A full electronic version will be published in the journal. Col 1: Julian year, Col 2: modified Julian date. Col 3: radial velocity corrected to local standard of rest. Col 4: radial velocity uncertainty. Col 5: residual. Col 6: star. Col 7: if noted, radial velocity reported in following reference.

(This table is available in its entirety in machine-readable form.)

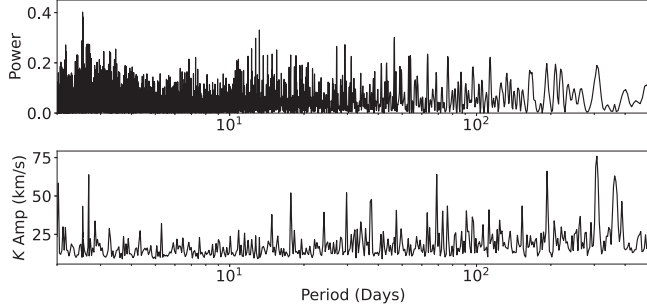


**Figure 5.** Top: Lomb–Scargle periodogram of S0-14’s residual radial velocity curve. Every period value sample has a corresponding Lomb–Scargle power. The significance of the peak power value is then calculated to determine if this period represents a detection. Bottom: 95% upper confidence limit on the amplitude of RV variations induced by a binary system ( $K$ ) as a function of the binary orbital period for S0-14.

signal relative to a nonperiodic data set taken at the same observation sampling and uncertainties.

The bootstrap false-alarm probability (FAP) is another way to test the significance of the signal in a slightly different view than the Monte Carlo simulations. VanderPlas (2018) explains how the FAP addresses the probability that a signal with no periodic component would lead to a peak of a given magnitude. We choose the bootstrap algorithm method in gatspy because it is the most robust estimate specifically of the FAP, compared to other methods given in gatspy (see VanderPlas 2018, for details). A similar bootstrap method was implemented by Gautam et al. (2019) to determine the FAP with Galactic center photometry data. To conduct this test, 10,000 Lomb–Scargle periodograms are simulated. Each of these periodograms is obtained by keeping the observation times and by drawing residual values randomly with replacement from the residual curve. The maxima of each resulting periodogram are computed. The peak periodogram power values from the data are compared to the distribution of power values from the bootstrap to determine the FAP. The bootstrap false-alarm test significance is then defined as 1—FAP and reported. This way, a higher value of 1—FAP (a lower FAP value) corresponds to a higher significance of a binary.

None of the stars’ residual curves have periodic variations beyond the  $3\sigma$  (99.7%) confidence limit using all three methods. While there is some variation in the significance values for some stars, the main importance is how the star performs in all three tests. A true binary system is expected to show high significance with all three tests. No star exhibits high significance across all methods, suggesting that no binary stars

have been detected. The detailed results from the Lomb–Scargle periodicity search are presented in Table 5.

### 5.2. Binary Curve Fitting

Another approach to search for a companion is through a Bayesian fit of the residual curve to the binary system curve. This is the same as the method described in Chu et al. (2018). The residual curves are fit with a binary star radial velocity model plus a constant. The following equation was used to model the radial velocity curve of an eccentric binary system (Hilditch 2001):

$$RV = K \frac{\sqrt{1 - e^2} \cos E \cos \omega - \sin E \sin \omega}{1 - e \cos E} + O, \quad (1)$$

with

$$K = \frac{2\pi a \sin i}{P}, \quad (2)$$

and where  $e$  is the binary eccentricity,  $\omega$  the argument of periastron,  $E$  the eccentric anomaly determined by solving the Kepler equation,  $i$  the inclination,  $P$  the period, and  $a$  the semimajor axis. This model is parameterized using the following five variables: the constant offset  $O$ , the radial velocity amplitude  $K$ , the eccentricity  $e$ , the argument of periastron  $\omega$ , and the mean longitude at J2000 (denoted as  $L_0$ ). The use of the mean longitude at J2000 is preferred to the usual time of closest approach, which is not bounded and not defined in cases of circular orbits (Hilditch 2001). For different fixed binary orbital periods  $P$ , this model is fit to the radial velocity residuals using a MultiNest sampler (Feroz & Hobson 2008; Feroz et al. 2009, 2019). A strong periodic signal at a given period would lead to a large, peaked value of  $K$  in the posterior. This method takes into account parameters such as eccentricity, which changes the shape of the curve from a perfect sinusoid wave. Periods from 2 to 500 days are uniformly sampled in log space. For S0-2, we followed the same methodology as in Chu et al. (2018), where we evenly spaced at 0.05 days for periods from 2 to 150 days because periods beyond 119 days are excluded by the binary stability criteria. Because of the more computationally expensive nature of this method, we did not sample periods as long as the Lomb–Scargle method. An example output of this methodology is shown for S0-14 in Figure 5, and the complete set of the  $K$  amplitude limit figures for the full sample is provided in Appendix C.

**Table 5**  
Companion Star Search Results

Star	Spectral Type	LS Amp Significance <sup>a</sup> (%)	Monte Carlo Significance <sup>a</sup> (%)	Bootstrap False-alarm Significance <sup>a</sup> (%)	Has Detected Companion	K Limit (km s <sup>-1</sup> )
S0-1	Early	89.64	92.34	99.94	No	44.2
S0-2	Early	69.30	72.00	80.32	No	8.5
S0-3	Early	75.80	94.70	90.03	No	23.9
S0-4	Early	82.73	92.50	98.66	No	56.4
S0-5	Early	65.42	94.88	98.52	No	38.4
S0-7	Early	96.11	93.80	92.38	No	62.9
S0-8	Early	75.54	96.40	99.79	No	50.7
S0-9	Early	85.06	95.90	92.38	No	41.5
S0-11	Early	79.26	90.20	86.80	No	38.7
S0-14	Early	82.03	98.60	70.99	No	15.7
S0-15	Early	85.95	93.50	33.37	No	56.5
S0-16	Early	90.52	67.00	99.27	No	82.4
S0-19	Early	56.10	64.00	99.73	No	50.1
S0-20	Early	67.17	96.60	52.88	No	90.4
S0-31	Early	79.38	100.00	42.34	No	75.7
S0-6	Late	76.83	97.18	44.18	No	3.1
S0-12	Late	85.69	99.00	94.57	No	3.9
S0-13	Late	84.13	90.50	86.34	No	3.4
S0-17	Late	60.64	75.00	99.90	No	21.1
S0-18	Late	99.57	97.80	73.03	No	21.1
S0-27	Late	97.65	90.30	52.30	No	20.5
S1-5	Late	90.88	92.70	4.47	No	4.75
S1-6	Late	95.54	96.30	63.66	No	11.7
S1-8	Early	96.92	90.40	29.82	No	59.2
S1-10	Late	85.08	99.00	95.40	No	6.9
S1-13	Late	99.74	100.00	45.61	No	41.4
S1-15	Late	92.29	93.20	46.69	No	7.9
S1-31	Late	88.97	82.50	51.89	No	17.7

**Notes.** Col 1: star name. Col 2: spectral type. Col 3: Lomb–Scargle model amplitude significance. Col 4: Monte Carlo simulation significance. Col 5: bootstrap false-alarm significance. Col 6: if companion was detected. Col 7:  $K$  amplitude limit.

<sup>a</sup> For the period with maximum Lomb–Scargle power.

(This table is available in machine-readable form.)

After calculating  $K$  upper limits for every sampled period, the median  $K$  value is then taken as a summary upper limit for the star. The limits on  $K$  amplitude are reported in Table 5. The  $K$  amplitude results for the sample are also shown in Figure 6. The  $K$  amplitude limits can be used to derive hypothetical companion mass limits and are reported in Appendix D. We do not report any detection of a binary system from this method, and these limits reflect our sensitivities to detecting binaries.

## 6. Binary Star Fraction Limits

Performing this systematic search for spectroscopic binaries has yielded no candidates, and we can use this result to place limits on the intrinsic binary population. To do this, one needs to make assumptions about the underlying binary star population. For the young, massive stars, we make use of the Sana et al. (2012) distributions of binary system parameters (mass ratios  $q$ , eccentricities, and periods). For the late-type stars, which are expected to be around  $1 M_{\odot}$ , we pull from the distributions reported by Raghavan et al. (2010). These distributions are used to create an initial estimate of the  $K$  amplitude distributions for both the massive star and solar-mass star binary populations, and we later explore variations in Appendix E, which show no impact for the early-type stars and a very modest impact for the late-type stars.

Parameters are drawn from the given distributions of  $\log P$ ,  $e$ , and mass ratio  $q$  from the given distributions. This is done

100,000 times to create a population of 100,000 binary systems. Using the binary mass equation:

$$M_{\text{comp}} \sin i = \left( \frac{PM_{\text{tot}}^2}{2\pi G} \right)^{1/3} K, \quad (3)$$

and inserting the drawn parameters, a distribution of  $K$  amplitudes are calculated for this simulated binary star population. When generating a binary system, we also make sure that the system does not result in a merger by calculating the minimum separation and ensuring it does not fall below the radius of the star ( $\sim 6 R_{\odot}$ ). With these simulated distributions for the two populations (see Figure 7), we can then use our  $K$  amplitude limits—and zero detections—to derive their binary fractions.

The calculated  $K$  amplitude distributions for massive and solar-mass stars is for a population made completely of binaries (a binary fraction of 100%). To make  $K$  amplitude distributions for binary fractions less than 100%, we replace the corresponding percentage of  $K$  values with 0 km s<sup>-1</sup>, representing the single star population. For example, a population with a binary fraction of 50% will have 50,000 values of 0 km s<sup>-1</sup>, and 50,000 values randomly drawn from the original simulated distribution.  $K$  amplitude distributions for different populations with binary fractions ranging from 10% to 100%, spaced

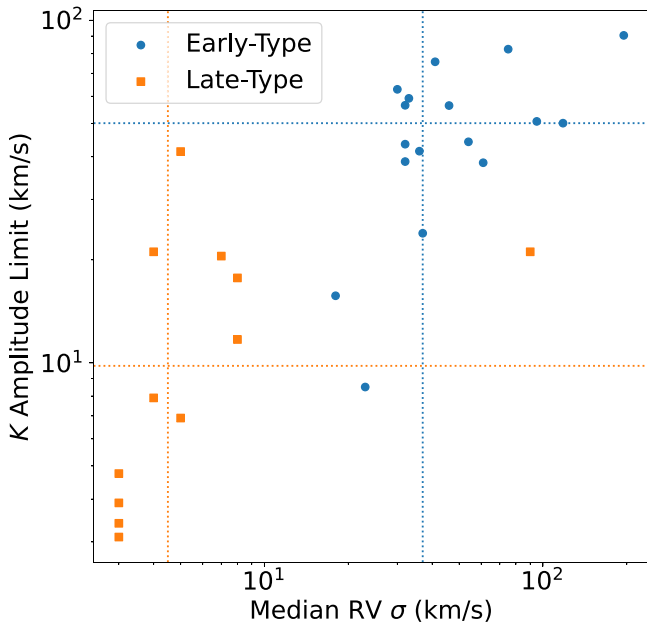


**Figure 6.** Median radial velocity uncertainty plotted with the  $K$  amplitude limit value for each star, color-coded by their spectral types. The  $K$  amplitude value comes from marginalizing the  $K$  amplitude limits over all sampled periods. The dashed lines represent the median values of the limits and radial velocity uncertainties for both the early-type and late-type stars.

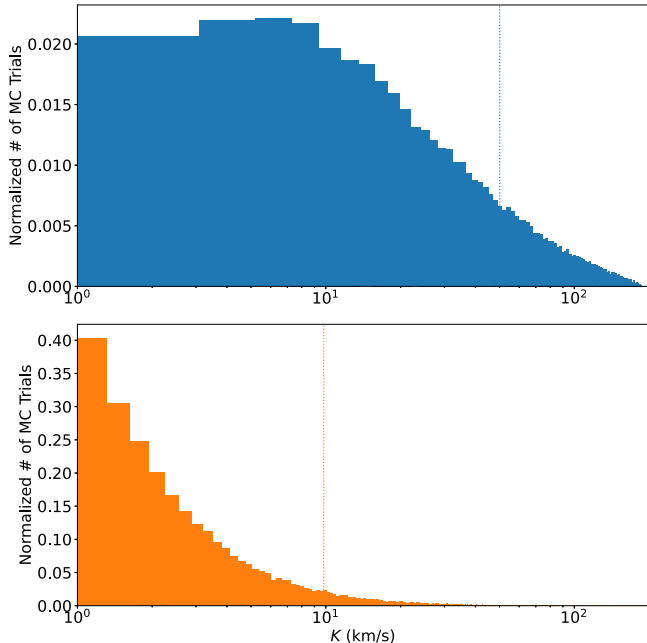


**Figure 7.** Top: Normalized  $K$  amplitude distributions for the simulated massive star binary population using Sana et al. (2012) parameters, along with the median  $K$  amplitude limit from the early-type sample (blue dotted line). Bottom: Normalized  $K$  amplitude distributions for the simulated solar-mass binary population using Raghavan et al. (2010) parameters, along with the median  $K$  amplitude limit from the late-type sample (orange dotted line). While the late-type sample has smaller  $K$  amplitude limits, they remain higher than the distribution of  $K$  amplitudes for the corresponding simulated binary star population.

evenly at 10%, are created. We also conduct finer sampling at binary fractions between 30% and 50%.

Once the adjusted  $K$  amplitude distribution is established, a simulation is run to determine how many simulated binary star

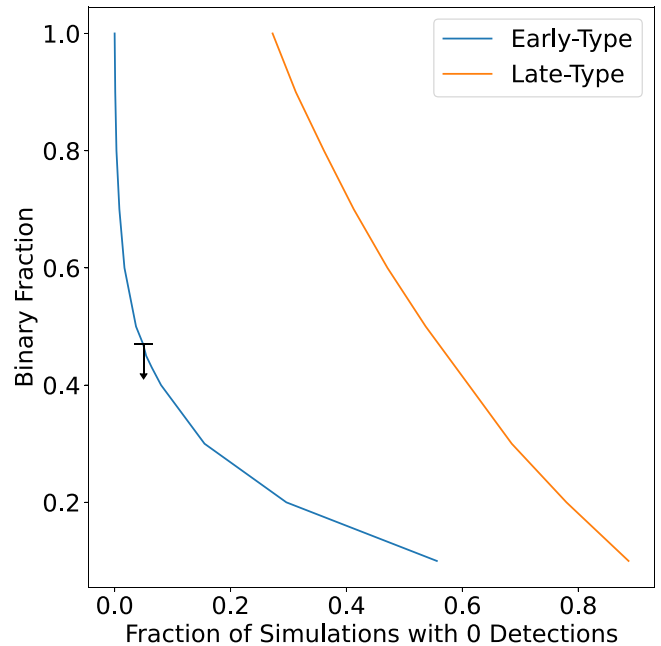


**Figure 8.** The simulated binary fraction populations vs. the fraction of Monte Carlo simulations with zero detections for each population of binary fractions, for both early-type and late-type stars. The binary fraction where we can place an upper limit at 95% confidence is the black arrow. The early-type star binary fraction limit is 47%. We cannot place a limit for the late-type stars. Our constraining power lies with the early-type stars, as the  $K$  amplitude distribution contains higher values of  $K$  compared to the late-type distribution.

systems would be detected, based on our  $K$  amplitude limits. For the early-type stars, the  $K$  limit from each of our 16 stars in Table 5 are compared to a randomly drawn  $K$  value from our massive star distribution, adjusted for binary fraction. If the  $K$  value drawn from the simulated population is higher than the limit from the sample star, we consider it a detection. For each simulation for the massive star population, there can be a minimum of zero detections and a maximum of 16 detections. This simulation is repeated 100,000 times for each different  $K$  amplitude distribution adjusted for binary fraction. The same process is done for the late-type stars, using the 12 late-type stars and solar-mass  $K$  amplitude distributions.

The fractions of simulations with zero detections for each adjusted  $K$  amplitude distribution are shown in Figure 8. For a massive star population with a 47% binary fraction, 5% of the simulations yielded zero detections. Based on this simulation and our zero binary detections, we can exclude a binary fraction greater than 47% for this population with a 95% confidence limit. For the solar-mass star populations, a constraint cannot be obtained, with even a 100% binary fraction only excluded at a 70% confidence limit.

## 7. Discussion

Our simulations have enabled us to place a limit on the young star population binary fraction at 47% (with 95% confidence). This is well below the binary fraction ( $70\% \pm 9\%$ ) for massive stars' larger galactic radii (Sana et al. 2012). Stephan et al. (2016) have estimated the decrease in the binary star fraction from evaporation and mergers via three-body interactions with the central black hole through the eccentric Kozai–Lidov effect. Figure 9 shows their simulation results at an age of 6 Myr, which we normalize to the observed binary

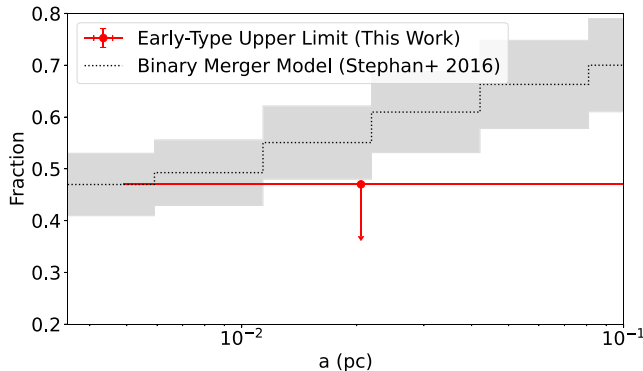


**Figure 9.** Binary fraction upper limit of 47% for the early-type star sample (red). The  $x$ -axis bar shows the range of the semimajor axis distribution. This limit is compared to the binary fraction model from Stephan et al. (2016) for a given semimajor axis from Sgr A\*, normalized to a starting binary fraction limit and uncertainty of  $70\% \pm 9\%$  for massive stars from Sana et al. (2012; gray shaded region). The binary fraction limit from this work for the young stars is consistent with the binary merger model and inconsistent with the binary fraction for massive stars in the solar neighborhood.

star fraction of 70% at large radii (shaded region). These predictions are consistent with our observations. We also note that the eclipsing binary fraction of stars outside the central arcsecond ( $\sim 0.4$  pc) reported by Gautam et al. (2019) is consistent with the field star binary fraction. The low binary fraction within  $\sim 20$  mpc appears to be explained well by a scenario in which the central SMBH drives binary star mergers near its proximity. The process has important implications for the production of gravitational wave sources (Abbott et al. 2016). Additional observations will further improve limits on the multiplicity of these stars closest to the SMBH.

This result of a low binary fraction is also consistent with the binary star disruption mechanism. In this evolution mechanism, a binary star system is tidally disrupted by the SMBH, leaving one single component bound to the SMBH (e.g., Hills 1988; Perets et al. 2007; Fragione et al. 2017; Generozov & Madigan 2020). The other component is ejected as a hypervelocity star, which have been observed in the Milky Way (see Brown 2015, for a review). It is also possible that a triple system may be disrupted by the SMBH and leave behind a captured binary S-star, so the discovery an S-star binary could support a disrupted triple-system hypothesis (Fragione & Gualandris 2018).

Naoz et al. (2018) explain that unaccounted binary stars can bias the inferred kinematic properties of the nearby clockwise disk of young stars. While the stars in this work are not members of the clockwise disk, it is interesting to compare the young S-stars to the disk population (e.g., Madigan et al. 2014). Given the closer proximity to the SMBH compared to the disk, the S-stars would be more sensitive to the effects of the SMBH. This closer proximity could lead to binary mergers and binary disruptions. Therefore, the S-star binary star fraction can be lower than the disk binary fraction.

It is not surprising that our binary fraction limit for the late-type stars is not as constraining as the limit for the early-type stars. The late-type stars'  $K$  amplitude distribution is dominated by very low values due to the binary population having longer periods and lower stellar masses. Even though we can place lower  $K$  amplitude limits for the individual late-type stars, given our better radial velocity precision, these lower limits do not outweigh the population's distribution of  $K$  amplitudes. Additionally, not identifying binary candidates among the late-

type stars is unsurprising. Stephan et al. (2016, 2019) reports that the evaporation timescale for a binary system with a total mass of  $2 M_{\odot}$  and separated by 3 au ( $P \sim 1300$  days) evaporates in under  $10^6$  yr. Because these late-type stars are  $\sim 1$  Gyr old, these stars have had sufficient time to evaporate, if they were previously part of binary star systems. Stephan et al. (2016) explain that, after a Gyr, there has been more time for mergers to take place—so even though, due to hardening interactions, binary star systems can survive longer than the evaporation time, these hardened, close binary stars can merge as they evolve off the main sequence.<sup>8</sup> Nevertheless, discovering binary star systems among the late-type star population would provide a strong constraint for the density of objects at the Galactic center (Rose et al. 2020), and continued monitoring will provide improved sensitivity for the late-type star population.

We are grateful for the helpful and constructive comments from the referee. We thank M. R. Morris for his comments and long-term efforts on the Galactic Center Orbits Initiative. The primary data for this work were collected with the W. M. Keck Observatory, which is operated as a scientific partnership among the California Institute of Technology, the University of California, and the National Aeronautics and Space Administration. We wish to recognize that the summit of Maunakea has always held a very significant cultural role for the indigenous Hawaiian community. We are most fortunate to have the opportunity to observe from this mountain. We also thank the staff of the Keck Observatory, especially Jim Lyke, Randy Campbell, Gary Puniwai, Heather Hershey, Hien Tran, Scott Dahm, Jason McIlroy, Joel Hicock, and Terry Stickel, for all their help in obtaining the new observations. Finally, we are grateful for the financial support for this work provided by NSF AST grants 1412615 and 1909554, the Gordon & Betty Moore Foundation, the Levine-Leichtman Family Foundation, Ken and Eileen Kaplan Student Support Fund, the Galactic Center Board of Advisors, and the Janet Marott Student Travel Awards. S.N. acknowledges the partial support from NASA ATP 80NSSC20K0505 and from NSF-AST 2206428 grants and thanks Howard and Astrid Preston for their generous support.

*Facilities:* W. M. Keck Observatory, Gemini North Observatory.

*Software:* Numpy (van der Walt et al. 2011; Harris et al. 2020), Astropy (Astropy Collaboration et al. 2013, 2018), Starkit (Kerzendorf & Do 2015), gatspy (VanderPlas & Ivezić 2015; VanderPlas 2018), IRAF (Tody 1986, 1993), Multinest (Feroz & Hobson 2008; Feroz et al. 2009, 2019), SPISEA (Hosek et al. 2020a; Hosek et al. 2020b), Scipy (Virtanen et al. 2020), OSIRIS Data Reduction Pipeline (Lyke et al. 2017; Lockhart et al. 2019).

## Appendix A Source Confusion

We took extra care to ensure that radial velocity measurements were not affected by either stellar or gaseous source confusion. Stellar source confusion affects 23 stars, which are therefore removed from the sample. Local gas can also affect the measurement of the Br $\gamma$  absorption line, because not only does it emit Br $\gamma$ , it does so at different velocities. One of the

<sup>8</sup> These merged stars would also appear younger by comparison.

**Table 6**  
Excluded Stars

Name	$K'$ (mag)	Spectral Type	R.A. $\Delta^a$ ( $''$ )	Decl. $\Delta^a$ ( $''$ )	R2D $^a$ ( $''$ )	Exclusion Reason
S0-24	15.58	Late	0.20	0.09	0.22	Confused
S0-26	15.20	Early	0.33	0.21	0.40	Confused
S0-53	15.50	Unknown	0.35	0.20	0.40	Confused
S0-28	15.45	Late	-0.14	-0.49	0.51	Too Few RVs
S0-62	15.37	Late	0.16	-0.54	0.57	Confused
S0-29	15.45	Late	0.37	-0.44	0.58	Confused
S0-67	15.49	Late	0.25	-0.54	0.59	Confused
S0-33	15.95	Unknown	0.65	-0.53	0.83	Confused
S0-32	14.08	Unknown	0.32	0.79	0.85	Foreground Star
S0-35	15.20	Unknown	0.02	0.88	0.88	Confused
S1-3	12.09	Early	0.32	0.88	0.94	Featureless
S1-26	15.41	Late	-0.88	0.39	0.96	Confused
S0-108	15.67	Unknown	0.45	-0.90	1.01	Confused
S1-2	14.64	Early	0.08	-1.02	1.02	Background Gas
S1-1	13.02	Early	1.04	0.03	1.04	Featureless
S1-27	15.80	Early	-1.03	0.19	1.05	Confused
S1-29	15.26	Early	1.07	0.16	1.08	Confused
S1-4	12.43	Early	0.88	-0.66	1.10	Featureless
S1-28	15.92	Late	-0.37	-1.05	1.12	Confused
irs16C	9.91	Early	1.05	0.55	1.18	Wolf-Rayet
S1-32	15.15	Late	-0.99	-0.66	1.19	Confused
S1-7	15.73	Late	-1.05	-0.58	1.20	Confused
S1-85	15.50	Unknown	0.92	-0.83	1.24	Confused
S1-33	14.94	Early	-1.25	-0.00	1.25	Background Gas
S1-86	15.30	Unknown	1.02	0.74	1.26	Confused
S1-12	13.41	Early	-0.75	-1.03	1.27	Featureless
S1-34	12.91	Late	0.87	-0.99	1.32	Confused
S1-14	12.90	Early	-1.32	-0.37	1.37	Featureless
irs16SW	9.98	Early	1.11	-0.95	1.46	Wolf-Rayet
S1-40	15.63	Unknown	-1.41	-0.61	1.54	Confused
S1-21	13.21	Early	-1.64	0.09	1.64	Featureless
S1-22	12.52	Early	-1.57	-0.52	1.65	Featureless
S1-51	14.91	Unknown	-1.66	-0.17	1.67	Confused
S1-45	15.19	Unknown	-1.28	1.10	1.69	Confused

**Note.**<sup>a</sup> From Sgr A\*.

(This table is available in machine-readable form.)

checks we conducted was to look at the strength of the gas emission at the star's radial velocity in the subtracted background. This led to the removal of two further stars, S1-2 and S1-33, because they were identified as having potentially biased radial velocity measurements based on their subtracted gas backgrounds. Table 6 provides the complete list of stars that were excluded from this analysis for all the reasons discussed in Section 2.

## Appendix B Impact of OSIRIS Detector Upgrade

Figure 10 compares the performance of the old and new detectors for a  $K \sim 14$  star from our standard Galactic Center observational setup. The new detector has enabled improved spectral signal-to-noise ratios for data for a given total integration time and FWHM.

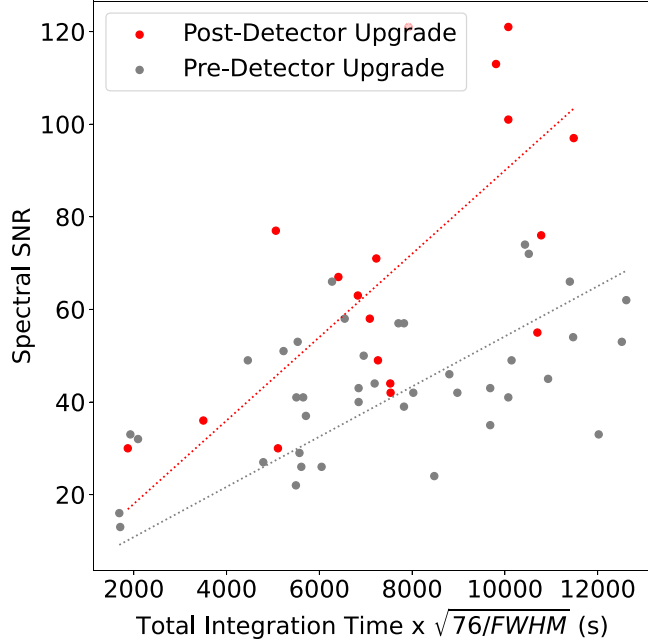


**Figure 10.** Spectral signal-to-noise ratio of a  $K' \sim 14$  mag star for a data set’s total integration time scaled by the data set’s FWHM relative to the average FWHM of 76 mas. Data taken with the newest OSIRIS detector and previous detector are plotted in red and gray, respectively. The dashed lines are fits to the data subsets. The steeper slope of the new detector data fit ( $9.00 \pm 0.69 \times 10^{-3}$ ) vs. the old detector data ( $5.42 \pm 0.29 \times 10^{-3}$ ) shows the improved spectral signal-to-noise ratio for a given integration time and FWHM.

### Appendix C Lomb–Scargle and $K$ Amplitude Limits

This appendix section presents the results discussed in Section 5. Figure 11 shows the Lomb–Scargle periodograms

for all stars used in the analysis, and Figure 12 shows the  $K$  amplitude limits per period.

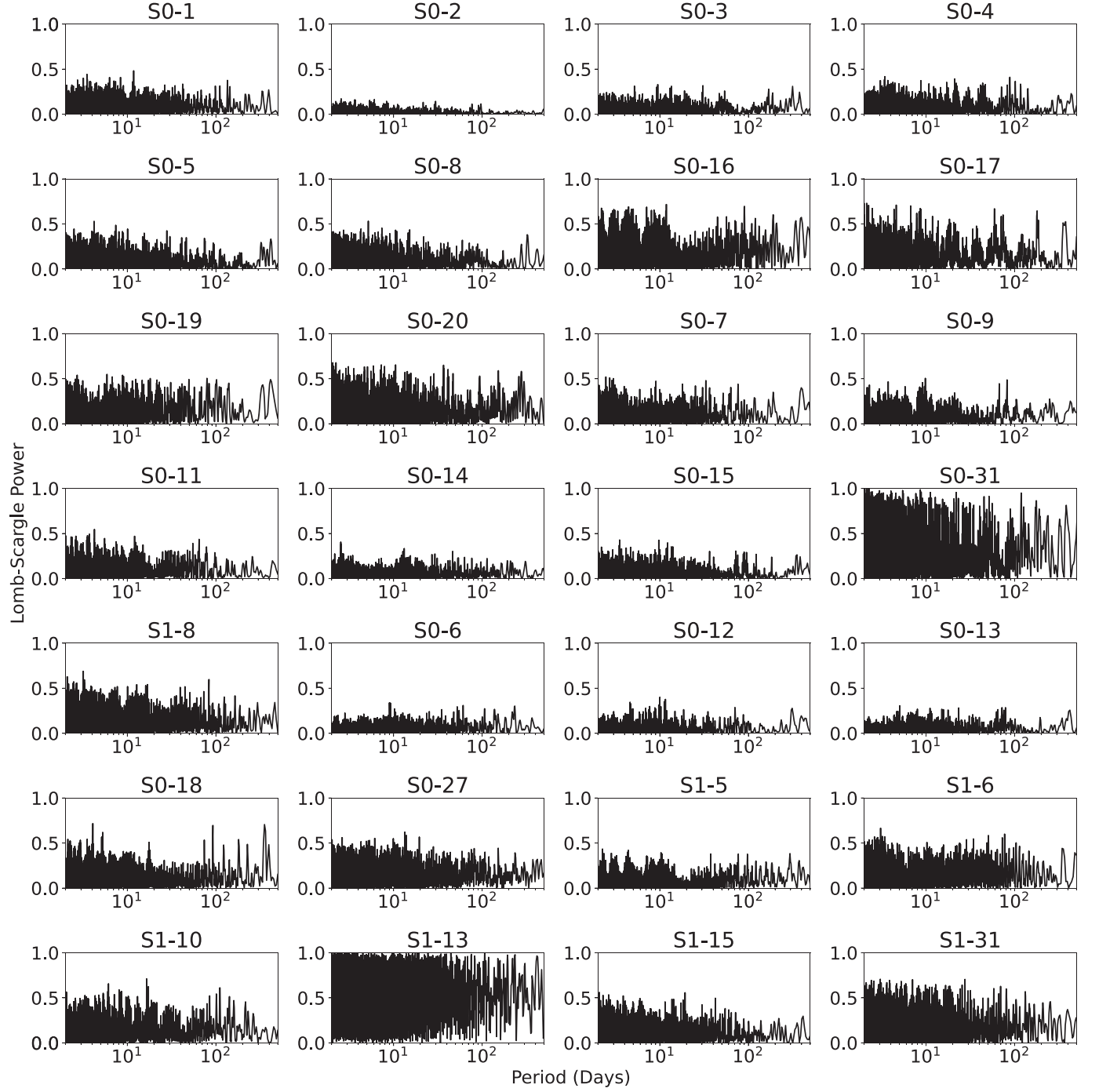


**Figure 11.** Lomb-Scargle periodograms for all 28 stars in the sample. For each plot, period in days is plotted on the x-axis, and the Lomb-Scargle power is on the y-axis.

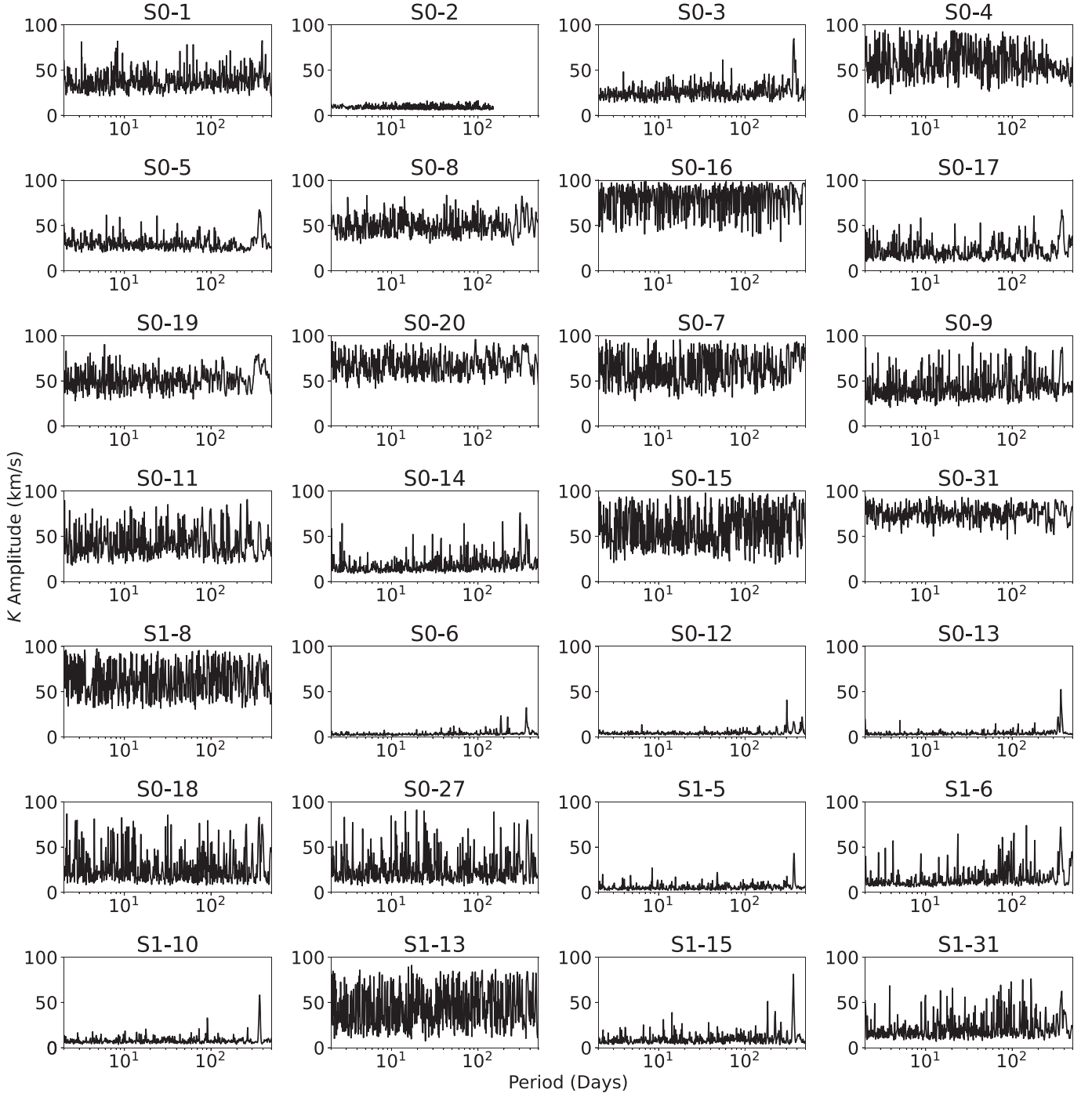


**Figure 12.**  $K$  amplitude limits for all 28 stars in the sample. For each plot, period in days is plotted on the  $x$ -axis, and the  $K$  amplitude limit in  $\text{km s}^{-1}$  is on the  $y$ -axis.

#### Appendix D Placing Limits on Companion Masses

With the results from the binary curve fitting, in particular our limits on the  $K$  amplitude, we move to place limits on hypothetical companion masses of binary systems using the same methodology as Chu et al. (2018). For each period  $P$ , there is a limit on  $K$ , and the binary mass equation (Equation (3)) can be solved assuming for a total mass, a limit for the companion mass for each period can be calculated. In order to determine the total mass for a star, we use its  $K'$  photometry reported Gautam et al. (2019) and an isochrone

generated with the SPISEA software (Hosek et al. 2020a; Hosek et al. 2020b). A 6.78 Myr isochrone is used for the early-type stars, and a 1 Gyr isochrone is used for the late-type stars. These isochrones use the MIST stellar evolution models (Choi et al. 2016), and each isochrone is corrected for extinction to the Galactic Center with a value of  $A_{K'} = 2.46$  (Schödel et al. 2010). Solar metallicities are used for both isochrones. These isochrones are shown in Figure 13. The total mass used for each star is given in Table 7. Habibi et al. (2017) reported masses for early-type S-stars in their analysis. For stars that overlap with our sample, their reported mass values

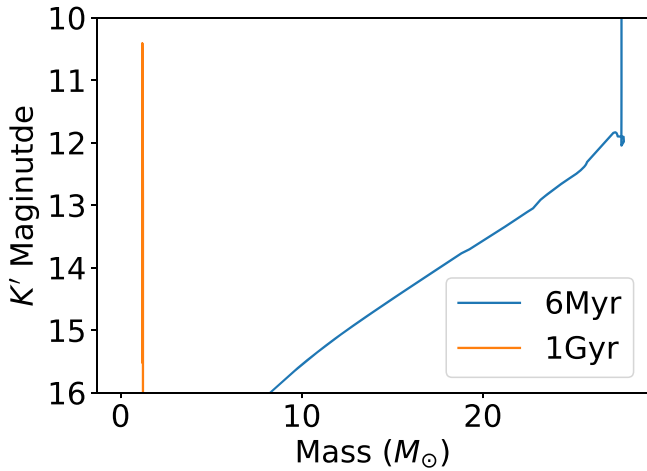


**Figure 13.** Two SPISEA isochrones used for determining the mass of a star based on its  $K'$  magnitude. The MIST stellar evolution models (Choi et al. 2016) and extinction law from (Schödel et al. 2010) are applied to these isochrones. The 6 Myr isochrone was used for the early-type stars, while the 1 Gyr isochrone was used for the late-type stars.

**Table 7**  
Companion Mass Limits

Star	Mean Mag ( $K'$ )	Spectral Type	Isochrone Mass ( $M_\odot$ )	Upper Limit $M_{\text{comp}}$ Mass ( $M_\odot$ )	Upper Limit Mass	Equal-mass Binary Ratio ( $M_\odot$ )
S1-5	12.48	Late	1.2	0.10	0.083	1.2
S0-13	13.24	Late	1.2	0.10	0.083	1.2
S0-15	13.55	Early	20.2	5.4	0.27	16.7
S0-14	13.57	Early	20.0	1.7	0.085	16.3
S0-6	13.95	Late	1.2	0.10	0.083	1.2
S1-13	13.96	Late	1.2	0.70	0.58	1.2
S0-2	14.02	Early	17.5	1.1	0.063	14.2
S1-15	14.04	Late	1.2	0.10	0.083	1.2
S1-8	14.08	Early	17.0	5.6	0.33	13.9
S0-4	14.15	Early	16.7	5.7	0.34	13.7
S0-9	14.24	Early	16.3	3.8	0.23	13.4
S0-12	14.27	Late	1.2	0.10	0.083	1.2
S0-3	14.53	Early	14.9	2.2	0.15	12.1
S1-10	14.66	Late	1.2	0.10	0.083	11.7
S0-1	14.68	Early	13.9	3.1	0.22	1.2
S0-18	14.92	Late	1.2	0.40	0.33	11.4
S0-5	14.97	Early	12.6	2.2	0.17	1.2
S0-31	15.03	Early	12.3	4.9	0.48	10.3
S0-7	15.12	Early	11.9	4.6	0.38	10.1
S0-11	15.13	Early	11.9	3.0	0.25	9.7
S0-16	15.3	Early	11.0	5.4	0.49	9.7
S0-19	15.36	Early	10.9	3.6	0.33	9.0
S1-6	15.38	Late	1.2	0.20	0.16	8.9
S0-27	15.54	Late	1.2	0.30	0.25	1.2
S1-31	15.59	Late	1.2	0.30	0.25	1.2
S0-8	15.79	Early	9.0	3.1	0.34	1.2
S0-20	15.85	Early	8.8	5.8	0.64	7.4
S0-17	15.85	Late	1.2	0.30	0.25	7.2

**Note.** Col 1: star name. Col 2: mean magnitude in  $K'$ . Col 3: spectral type. Col 4: mass from the isochrone. Col 5: upper limit on companion mass. Col 6: upper limit on the mass ratio. Col 7: mass of each component of an equal-mass binary system that would emit the same flux as the star's photometry.

(This table is available in machine-readable form.)

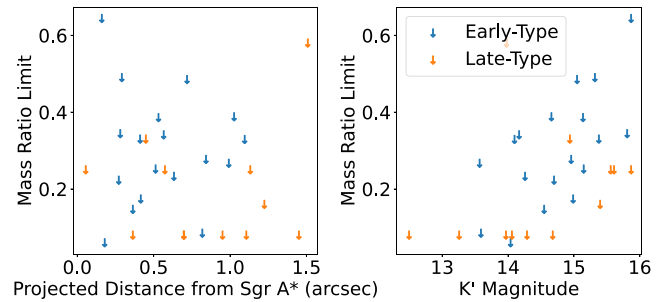


**Figure 14.** Left: Companion mass limits for each star plotted with their projected distance from Sgr A\*. These limits come from marginalizing the mass limits over all sampled periods. Right: Companion mass limits for each star plotted with their  $K'$  magnitude.

are lower than the isochrone mass values but still consistent within  $2\sigma$ . We report the median upper limits for the companion masses for all periods in Table 7 and Figure 14.

The photometric information from Gautam et al. (2019) for each star is used to place conservative limits on the masses of an equal-mass binary system. To do this, the total flux from the star is divided in half. The SPISEA isochrone is then searched to find the mass of a star that would contribute the equivalent amount of flux. This places a limit on the components of a face-on binary system composed of equal-mass stars. This can be thought of as a conservative limit, because the spectral differences between different mass stars are not considered in this part of the analysis. These limits are reported in Table 7.

## Appendix E Effect of Period Distributions and Sample Size on Simulations

We note that, while we adopt field-like distributions for the binaries, there are processes that truncate long-period binaries in the dense environment of the Galactic center compared to the field. For example, flyby stars unbind widely separated binaries (e.g., Binney & Tremaine 2011; Rose et al. 2020; see the latter for unbinding of eccentric binaries), which produces a distribution described by Stephan et al. (2016, 2019). Furthermore, stability and the Hills process tend to truncate the distribution in a similar manner. Thus, it can be estimated as log-uniform in the literature (e.g., Fragione & Antonini 2019). It should be noted that the Sana et al. (2012) distribution, adopted here for the early-type stars, favors short-period distribution, consistent with the unbinding processes (as noted in Hoang et al. 2018). We examine the impact of these effects on our results by testing two period distributions for the young stars: (1) the Sana et al. (2012) period distribution truncated at  $9.8 \times 10^4$  days, (2) a log-normal distribution truncated at the same length. We find that both of these period distributions produce no impact on our inference about the binary fraction. The binary fraction limit changes by less than 3%. The effects of these period distributions are shown in Figure 15.

For late-type stars, the binary distribution makes a modest difference in the resulting binary fraction limit, because the Raghavan et al. (2010) distribution extends to very long periods that these dynamical processes will truncate. To approximate these effects, we use the results of the simulations from Stephan et al. (2016), which shows a truncated period distribution at  $3.3 \times 10^5$  days for  $1.2 M_\odot$  stars. If the late-type star binary population is truncated, then our data has a modest

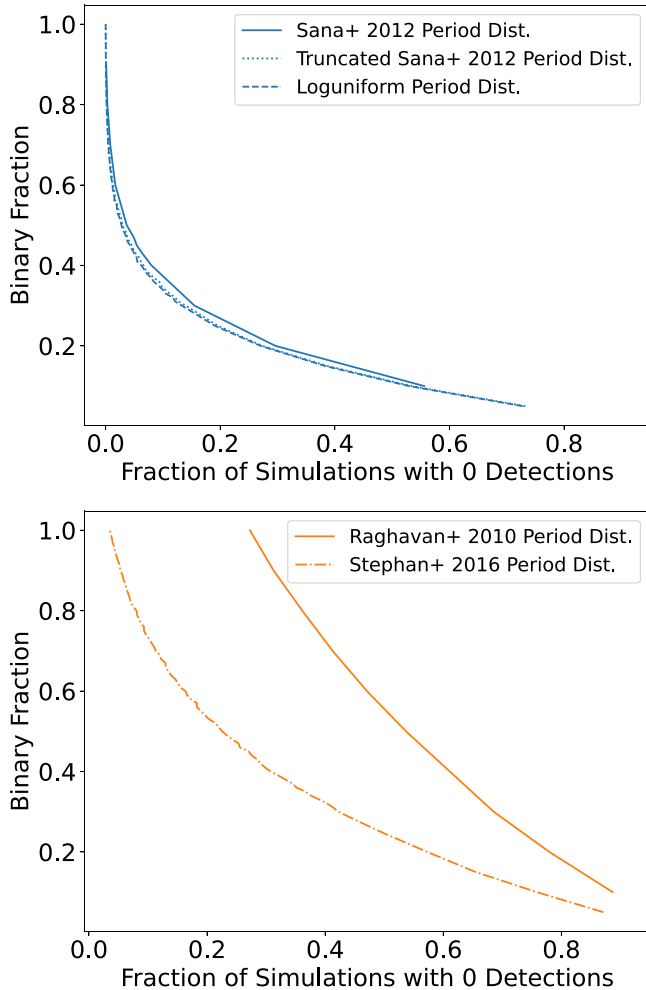


**Figure 15.** The simulated binary fraction populations vs. the fraction of Monte Carlo simulations with zero detections for each population of binary fractions with different period distributions. Left: The early-type star simulations when using the following period distributions: Sana et al. (2012), truncated Sana et al. (2012), and log-uniform. The binary fraction limit changes by less than 3%. Right: The late-type star simulations when using the Raghavan et al. (2010) and Stephan et al. (2016) period distributions. The Stephan et al. (2016) distribution truncates the longer-period binaries compared to Raghavan et al. (2010). We would infer a binary fraction less than 93% at 95% confidence with the Stephan et al. (2016) distribution.

constraint on the binary fraction. We would infer an upper limit of the binary fraction to be less than 93% at 95% confidence.

We have also explored our sensitivity to sample size for our simulations. To account for an increased sample size, we double-count stars from our observational sample and compare them to the simulated populations. For the young stars, it would take an increase of eight stars (from 16 to 24) to decrease the binary fraction limit by 10%. Changing the sample by one or two stars for the early-type stars does not dramatically affect the limit.

## ORCID iDs

- Devin S. Chu <https://orcid.org/0000-0003-3765-8001>  
 Tuan Do <https://orcid.org/0000-0001-9554-6062>  
 Andrea Ghez <https://orcid.org/0000-0003-3230-5055>  
 Abhimat K. Gautam <https://orcid.org/0000-0002-2836-117X>  
 Anna Ciurlo <https://orcid.org/0000-0001-5800-3093>  
 Kelly Kosmo O’Neil <https://orcid.org/0000-0003-2400-7322>

- Matthew W. Hosek, Jr. <https://orcid.org/0000-0003-2874-1196>  
 Aurélien Hees <https://orcid.org/0000-0002-2186-644X>  
 Smadar Naoz <https://orcid.org/0000-0002-9802-9279>  
 Shoko Sakai <https://orcid.org/0000-0001-5972-663X>  
 Jessica R. Lu <https://orcid.org/0000-0001-9611-0009>  
 Zhuo Chen (陈卓) <https://orcid.org/0000-0002-3038-3896>  
 Rory O. Bentley <https://orcid.org/0000-0001-7017-8582>

## References

- Abbott, B. P., Abbott, R., Abbott, T. D., et al. 2016, *PhRvL*, **116**, 061102  
 Astropy Collaboration, Price-Whelan, A. M., Sipőcz, B. M., et al. 2018, *AJ*, **156**, 123  
 Astropy Collaboration, Robitaille, T. P., Tollerud, E. J., et al. 2013, *A&A*, **558**, A33  
 Binney, J., & Tremaine, S. 2011, Galactic Dynamics: Second Edition (Princeton, NJ: Princeton Univ. Press)  
 Boehle, A., Ghez, A. M., Schödel, R., et al. 2016a, *ApJ*, **830**, 17  
 Boehle, A., Larkin, J. E., Adkins, S. M., et al. 2016b, *Proc. SPIE*, **9908**, 99082Q  
 Bohlin, R. C., Mészáros, S., Fleming, S. W., et al. 2017, *AJ*, **153**, 234  
 Brown, W. R. 2015, *ARA&A*, **53**, 15  
 Choi, J., Dotter, A., Conroy, C., et al. 2016, *ApJ*, **823**, 102  
 Chu, D. S., Do, T., Hees, A., et al. 2018, *ApJ*, **854**, 12  
 Ciurlo, A., Campbell, R. D., Morris, M. R., et al. 2020, *Natur*, **577**, 337  
 Do, T., Hees, A., Ghez, A., et al. 2019, *Sci*, **365**, 664  
 Duchêne, G., & Kraus, A. 2013, *ARA&A*, **51**, 269  
 Eisenhauer, F., Genzel, R., Alexander, T., et al. 2005, *ApJ*, **628**, 246  
 Feroz, F., & Hobson, M. P. 2008, *MNRAS*, **384**, 449  
 Feroz, F., Hobson, M. P., & Bridges, M. 2009, *MNRAS*, **398**, 1601  
 Feroz, F., Hobson, M. P., Cameron, E., & Pettitt, A. N. 2019, *OJAp*, **2**, 10  
 Fragione, G., & Antonini, F. 2019, *MNRAS*, **488**, 728  
 Fragione, G., Capuzzo-Dolcetta, & Kroupa, P. 2017, *MNRAS*, **467**, 451  
 Fragione, G., & Gualandris, A. 2018, *MNRAS*, **475**, 4986  
 Gautam, A. K., Do, T., Ghez, A. M., et al. 2019, *ApJ*, **871**, 103  
 Generozov, A., & Madigan, A.-M. 2020, *ApJ*, **896**, 137  
 Ghez, A. M., Duchêne, G., Matthews, K., et al. 2003, *ApJL*, **586**, L127  
 Ghez, A. M., Salim, S., Weinberg, N. N., et al. 2008, *ApJ*, **689**, 1044  
 Gillessen, S., Plewa, P. M., Eisenhauer, F., et al. 2017, *ApJ*, **837**, 30  
 Habibi, M., Gillessen, S., Martins, F., et al. 2017, *ApJ*, **847**, 120  
 Harris, C. R., Millman, K. J., van der Walt, S. J., et al. 2020, *Natur*, **585**, 357  
 Hilditch, R. W. 2001, An Introduction to Close Binary Stars (Cambridge: Cambridge Univ. Press), 392  
 Hills, J. G. 1988, *Natur*, **331**, 687  
 Hoang, B.-M., Naoz, S., Kocsis, B., Rasio, F. A., & Dosopoulou, F. 2018, *ApJ*, **856**, 140  
 Hosek, M. W. J., Lu, J. R., Lam, C. Y., et al. 2020a, SPISEA: Stellar Population Interface for Stellar Evolution and Atmospheres, Astrophysics Source Code Library, ascl:[2006.016](#)  
 Hosek, M. W. J., Lu, J. R., Lam, C. Y., et al. 2020b, *AJ*, **160**, 143  
 Kerr, F. J., & Lynden-Bell, D. 1986, *MNRAS*, **221**, 1023  
 Kerzendorf, W., & Do, T. 2015, starkit: First Real Release, v0.2, Zenodo, doi:[10.5281/zenodo.28016](#)  
 Larkin, J., Barczys, M., Krabbe, A., et al. 2006, *NewAR*, **50**, 362  
 Levin, Y. 2007, *MNRAS*, **374**, 515  
 Lockhart, K. E., Do, T., Larkin, J. E., et al. 2019, *AJ*, **157**, 75  
 Löffler, U., Baumgardt, H., & Kroupa, P. 2008, *ApJL*, **683**, L151  
 Lomb, N. R. 1976, *Ap&SS*, **39**, 447  
 Lyke, J., Do, T., Boehle, A., et al. 2017, OSIRIS Toolbox: OH-Suppressing InfraRed Imaging Spectrograph pipeline. ascl, Astrophysics Source Code Library, ascl:[1710.021](#)  
 Madigan, A.-M., Pfuhl, O., Levin, Y., et al. 2014, *ApJ*, **784**, 23  
 Martins, F., Trippe, S., Paumard, T., et al. 2006, *ApJL*, **649**, L103  
 McGregor, P. J., Hart, J., Conroy, P. G., et al. 2003, *Proc. SPIE*, **4841**, 1581  
 Merritt, D., Gualandris, A., & Mikkola, S. 2009, *ApJL*, **693**, L35  
 Mieda, E., Wright, S. A., Larkin, J. E., et al. 2014, *PASP*, **126**, 250  
 Morris, M. 1993, *ApJ*, **408**, 496  
 Naoz, S., Ghez, A. M., Hees, A., et al. 2018, *ApJ*, **853**, L24  
 Ott, T., Eckart, A., & Genzel, R. 1999, *ApJ*, **523**, 248  
 Perets, H. B., Hopman, C., & Alexander, T. 2007, *ApJ*, **656**, 709  
 Pfuhl, O., Alexander, T., Gillessen, S., et al. 2014, *ApJ*, **782**, 101  
 Rafelski, M., Ghez, A. M., Hornstein, S. D., Lu, J. R., & Morris, M. 2007, *ApJ*, **659**, 1241  
 Raghavan, D., McAlister, H. A., Henry, T. J., et al. 2010, *ApJS*, **190**, 1

- Rose, S. C., Naoz, S., Gautam, A. K., et al. 2020, [ApJ](#), **904**, 113  
 Sana, H., de Mink, S. E., de Koter, A., et al. 2012, [Sci](#), **337**, 444  
 Scargle, J. D. 1982, [ApJ](#), **263**, 835  
 Schödel, R., Najarro, F., Muzic, K., & Eckart, A. 2010, [A&A](#), **511**, A18  
 Stephan, A. P., Naoz, S., Ghez, A. M., et al. 2016, [MNRAS](#), **460**, 3494  
 Stephan, A. P., Naoz, S., Ghez, A. M., et al. 2019, [ApJ](#), **878**, 58  
 Tody, D. 1986, [Proc. SPIE](#), **627**, 733  
 Tody, D. 1993, in ASP Conf. Ser. 52, Astronomical Data Analysis Software and Systems II, ed. R. J. Hanisch, R. J. V. Brissenden, & J. Barnes (San Francisco, CA: ASP), [173](#)  
 van Dam, M. A., Bouchez, A. H., Le Mignant, D., et al. 2006, [PASP](#), **118**, 310  
 van der Walt, S., Colbert, S. C., & Varoquaux, G. 2011, [CSE](#), **13**, 22  
 Vanderplas, J., Naul, B., Willmer, A., Williams, P., & Morris, B. M. 2016, gatspy: v0.3 Feature Release, Zenodo, doi:[10.5281/zenodo.47887](#)  
 VanderPlas, J. T., & Ivezić, Ž. 2015, [ApJ](#), **812**, 18  
 VanderPlas, J. T. 2018, [ApJS](#), **236**, 16  
 Virtanen, P., Gommers, R., Oliphant, T. E., et al. 2020, [NatMe](#), **17**, 261  
 Witzel, G., Ghez, A. M., Morris, M. R., et al. 2014, [ApJL](#), **796**, L8  
 Wizinowich, P. L., Le Mignant, D., Bouchez, A. H., et al. 2006, [PASP](#), **118**, 297